Document Version
Final published version

Citation (APA)
van der Sar, S. J., Leibold, D., & Schaart, D. R. (2026). Experimental investigation of the potential of LaBr3:Ce, LYSO:Ce, and YAP:Ce for scintillator-based x-ray photon-counting detectors. *Physics in medicine and biology*, *71*(2), Article 025003. https://doi.org/10.1088/1361-6560/ae1bf4

Physics in Medicine & Biology

Experimental investigation of the potential of $LaBr_3$:Ce, LYSO:Ce, and YAP:Ce for scintillator-based x-ray photon-counting detectors

To cite this article: Stefan J van der Sar *et al* 2026 *Phys. Med. Biol.* **71** 025003

IOP Publishing   *Phys. Med. Biol.* **71** (2026) 025003   https://doi.org/10.1088/1361-6560/ae1bf4

Physics in Medicine & Biology

IPEM
Institute of Physics and Engineering in Medicine

RECEIVED
7 April 2025

REVISED
30 October 2025

ACCEPTED FOR PUBLICATION
5 November 2025

PUBLISHED
20 January 2026

PAPER

Experimental investigation of the potential of $LaBr_3$:Ce, LYSO:Ce, and YAP:Ce for scintillator-based x-ray photon-counting detectors

Stefan J van der Sar[1,*], **David Leibold**[1] and **Dennis R Schaart**[1,2,*]

[1] Department of Radiation Science and Technology, Delft University of Technology, Delft, The Netherlands
[2] Holland Proton Therapy Center, Delft, The Netherlands
[*] Authors to whom any correspondence should be addressed.

E-mail: s.j.vandersar@tudelft.nl and d.r.schaart@tudelft.nl

Keywords: count-rate capability, energy resolution, scintillation detectors, silicon photomultipliers, photon-counting CT

Abstract

Objective. We investigate scintillation detectors with silicon photomultipliers (SiPMs) as alternatives to direct-conversion detectors based on CdTe/$Cd_{1-x}Zn_xTe$ (CZT) for x-ray photon-counting imaging. Here, we measure counting and spectral performance of three scintillators and compare the results with performances reported in literature for CdTe/CZT detectors for diagnostic photon-counting computed tomography (PCCT). *Approach.* We built 1×1 mm^2 single-pixel detectors by coupling readily available LYSO:Ce, YAP:Ce, and $LaBr_3$:Ce scintillators to ultrafast SiPMs. Pulse processing was optimized for rate capability rather than energy resolution. We exposed the detectors to three radioisotopes to determine energy response proportionality and energy resolution. Using an x-ray tube, we measured x-ray spectra and count rate curves, i.e. output count rate (OCR) versus input count rate (ICR). *Main results.* The energy resolutions of the LYSO:Ce and YAP:Ce detectors exceed 30% full-width-at-half-maximum (FWHM) at 60 keV, with YAP:Ce showing a more proportional response. For a 30 keV count-detection threshold, the maximum OCR of the YAP:Ce detector is 5.4 Mcps pixel^{-1} for paralyzable-like counting, while the OCR approaches 12.5 Mcps pixel^{-1} for nonparalyzable-like counting. The LYSO:Ce detector reaches 4.5 Mcps pixel^{-1} and 10 Mcps pixel^{-1}, respectively, and the $LaBr_3$:Ce detector 10.4 Mcps pixel^{-1} and 22 Mcps pixel^{-1}. Thereby, the rate capability of the $LaBr_3$:Ce detector is almost 80% of that reported for two CdTe/CZT detectors for diagnostic PCCT. Moreover, the $LaBr_3$:Ce detector has high proportionality and an energy resolution of about 20% FWHM at 60 keV, which is comparable to at least one CdTe detector for diagnostic PCCT. The x-ray tube spectra measured using the scintillation detectors show reasonable agreement with incident spectra. *Significance.* This work indicates that $LaBr_3$:Ce-based detectors may become an alternative to direct-conversion detectors for diagnostic PCCT, whereas LYSO:Ce- and YAP:Ce-based detectors appear better suited for applications with lower ICR, e.g. cone-beam PCCT in radiotherapy. Ways to further improve x-ray photon-counting scintillation detectors are also discussed.

1. Introduction

Photon-counting detectors (PCDs) for medical x-ray imaging count the number of x-ray photons impinging on each detector pixel. Based on a measurement of the energy deposited by each photon, each count is also registered in one of typically 2–8 energy bins that cover the x-ray spectrum of interest. PCDs can increase the contrast-to-noise ratio, and/or reduce the radiation dose and contrast agent load that come with traditional x-ray imaging systems equipped with energy-integrating detectors. Moreover, they facilitate conventional dual-energy imaging and enable innovative multi-energy imaging, which allows for quantitative imaging of (multiple) contrast agents, including ones with a very high atomic number ($Z > 60$, K-edge imaging), in a single acquisition (Leng *et al* 2019, Flohr *et al* 2020, Danielsson *et al* 2021).

Most PCDs developed to date are direct-conversion detectors consisting of the semiconductors CdTe or $Cd_{1-x}Zn_xTe$ (CZT, $x \approx 0.1$–0.2), and x-ray computed tomography (CT) systems that are employing CdTe/CZT detectors and that are capable of patient scanning have been built (Si-Mohamed *et al* 2021, Rajendran *et al* 2022). In such a detector, an x-ray photon is directly converted into electric charges, which migrate to a pixelated electrode due to the bias voltage applied to the CdTe/CZT layer, ideally inducing a current pulse on one of the electrode pixels. CdTe and CZT have a reasonably high density ($\rho \approx 5.8$ g cm^{-3}) and effective atomic number ($Z_{\mathrm{eff}} \approx 50$), so that a detector thickness of 1.5–3.0 mm offers sufficient detection efficiency in the energy range of medical x-ray imaging ($E < 150$ keV). Also, these detectors produce short pulses (tens of ns after pulse processing/shaping) and a reduction of the pixel size to 0.5×0.5 mm^2 or smaller is feasible in practice. Both help to reduce the detrimental effects of pulse pile-up, such as a loss of counts and incorrect energy measurement. This is needed because of the high fluence rates in medical x-ray imaging, which can exceed 10^8 photons s^{-1} mm^{-2} in a very demanding modality such as diagnostic CT (Persson *et al* 2016). However, reliable and stable detector operation at high fluence rates demands CdTe/CZT detectors with few charge trapping centers, homogeneously distributed in the detector (Roy *et al* 2019, Flohr *et al* 2020). The cost-effective production and wide availability of such detector-grade material remain points of concern. Another issue is the degradation of performance in spectral imaging tasks, mainly due to charge sharing (Taguchi *et al* 2024, Stierstorfer and Hupfer 2025). Charge sharing refers to charges created in one x-ray interaction in the detector inducing pulses on multiple electrode pixels. It increases with decreasing pixel size.

The investigation of other types of detector thus appears warranted. One such alternative is a silicon-based direct conversion detector. However, Si has a much lower density (2.3 g cm^{-3}) and Z_{eff} (14) than CdTe/CZT. Consequently, 3.0–6.0 cm of material is needed for dose-efficient imaging. On the one hand, this had led to a detector design that substantially reduces pile-up and charge sharing (Bornefalk and Danielsson 2010). On the other hand, such a big volume of high-quality Si increases costs. Moreover, Compton scatter is the dominant interaction mechanism in Si detectors, which is detrimental to spectral imaging (Taguchi *et al* 2024, Stierstorfer and Hupfer 2025). Nonetheless, a CT system with Si detectors capable of patient scanning has been built (Da Silva *et al* 2019).

As another alternative, we work on indirect-conversion detectors. In such detectors, each pixel consists of a scintillation material, which converts an x-ray photon into a pulse of optical photons, and a light sensor, which converts the scintillation photons into electric charges. Traditionally, there are reflectors between pixels, which practically eliminate light sharing (cf. charge sharing). Our choice of light sensor is the silicon photomultiplier (SiPM), which provides internal gain, thereby lifting the signal generated by a single x-ray photon above the noise level of the readout electronics. In addition, SiPMs can be miniaturized to sub-mm sizes. Various scintillators that combine high density and Z_{eff} with a fast response to incoming radiation are widely available. Since the detector relies on the transport of optical photons rather than electric charges, it may be easier to synthesize detector-grade materials in a cost-effective way. This claim is supported by the fact that the vast majority of detectors in present-day medical imaging systems are scintillation detectors. Similarly, SiPMs have made it into clinical systems, e.g. the positron emission tomography scanners of all major vendors (Surti and Karp 2020).

In first order, the response of an SiPM-based scintillation detector can be described as follows. When an x-ray photon deposits an amount of energy E (in keV) in a scintillation crystal, the mean number of generated scintillation photons equals E times the light yield Y in photons/keV. The actual number of scintillation photons per event typically shows a different (usually greater) variance than expected from Poisson statistics. The deviation from a Poisson distribution is more pronounced for a scintillator that exhibits a higher degree of non-proportionality, i.e. a stronger dependency of Y on E (Dorenbos *et al* 1995, Khodyuk and Dorenbos 2012). Only a fraction of the scintillation photons is detected by the SiPM (limited light collection and photon detection efficiencies), and the statistics of the detected scintillation photons affects the energy resolution.

The chance that a scintillation photon is detected at a time t_0 after the x-ray photon interacted in the scintillator is, in the simplest case, proportional to $\exp(-t_0/\tau_{\mathrm{d}})$, τ_{d} being the scintillator's decay time constant. The photon is detected by one of the light-sensitive elements of the SiPM, a single-photon avalanche diode (SPAD), which generates a current pulse that is approximately proportional to $\exp(-(t\text{–}t_0)/\tau_{\mathrm{r}})$ provided $t\text{–}t_0 \geqslant 0$. Here, τ_{r} is the recharge time constant. Since the SPADs on a single SiPM are connected in parallel, the pulse produced by an SiPM-based scintillation detector in response to an x-ray photon is the convolution of these two exponential functions, although with statistical fluctuations due to the limited number of scintillation photons detected per unit time (Van der Sar *et al* 2021).

Our goal in this work is to evaluate experimentally the counting and spectral performance of three 1×1 mm^2 single-pixel x-ray PCDs consisting of an ultrafast SiPM ($\tau_{\mathrm{r}} \leqslant 9$ ns) coupled to either a LYSO:Ce, YAP:Ce, or $LaBr_3$:Ce scintillation crystal. These scintillators have a lower value of τ_{d}, and thus better counting potential, than scintillators explored by others for photon-counting applications (Sagisaka *et al* 2023, Shimazoe *et al* 2023). We optimize pulse processing for count rate capability rather than energy resolution, and measure count rate curves and energy spectra using an x-ray tube, and energy resolutions at 60 keV using an Am-241 source. These measurements are then compared to those found in literature for direct-conversion detectors developed for photon-counting CT. It is noted that preliminary results of this work have been presented elsewhere (Van der Sar *et al* 2022a, Van der Sar *et al* 2022b). In this paper, we provide the details of constructing the prototype detectors, extend the count rate curves of the $LaBr_3$:Ce detector to an incident fluence rate of 10^8 photons per pixel per second, and not only show Am-241 spectra (60 keV), but also Ba-133 (32 and 81 keV) and Co-57 (14 and 122 keV) spectra for all three detectors, which allows for a more complete assessment of the spectral capabilities of the detectors.

2. Method

2.1. Detectors

We built single-pixel detectors based on 1.5 mm thick $Lu_{1.8}Y_{0.2}SiO_5$:Ce (LYSO:Ce, from Project Shanghai Crystals), 4.5 mm thick $YAlO_3$:Ce (YAP:Ce, from Crytur) and 3.5 mm thick $LaBr_3$:Ce ($LaBr_3$:Ce, from Luxium Solutions, formerly Saint Gobain Crystals) scintillation crystals, all with a cross-sectional area of 1×1 mm^2. Table 1 shows a few relevant properties of these scintillators, as specified by major scintillator manufacturers.

Each scintillation crystal was coupled to a 1×1 mm^2 ultrafast SiPM from Broadcom (see figure 1(a)). These SiPMs are based on the company's commercially available near-ultraviolet high-density (NUV-HD) technology, but feature a reduced SPAD pitch of 15 μm and adjusted quenching resistors, so that, at a bias voltage of 34 V, i.e. at 7 V above the breakdown voltage, they exhibit a recharge time constant of 7 ns (YAP:Ce and $LaBr_3$:Ce detectors) or 9 ns (LYSO:Ce detector), an internal gain of about 8×10^5, an (optical) photon detection efficiency (PDE) of about 20%–30% in the relevant wavelength range, a dark count rate in the order of 0.1 Mcps per mm^2 (also see section 3.1), a crosstalk probability below 10%, and negligible afterpulsing (<1%). More information on these SiPM properties can be found in review papers, e.g. (Piemonte and Gola 2019) and (Schaart 2021).

We used Norland Optical Adhesive 63 (NOA 63) for the LYSO:Ce detector and NOA 88 for the YAP:Ce detector to make an optical coupling between scintillation crystal and SiPM. The two adhesives were selected because of their optimal transmittance at the emission wavelengths of each scintillator. Since $LaBr_3$:Ce is a hygroscopic scintillator, the $LaBr_3$:Ce detector was built in a glovebox with a dry nitrogen atmosphere, and the very low outgassing, optically transparent MasterBond EP30-2 epoxy was used for the optical coupling. As shown in figure 1(b), we subsequently covered the crystals in highly reflective polytetrafluoroethylene (Teflon) powder, which we compressed to increase the light collection efficiency on the SiPM. Lastly, we sealed the $LaBr_3$:Ce detector using a two-component epoxy, so that we were able to conduct experiments outside the glovebox with this detector. See figure 1(c) for a picture of the resulting detector, and figure 1(d) for a schematic drawing.

2.2. Signal processing

The detectors were connected to Broadcom's AFBR-S4E001 evaluation board, which has a 166 V A^{-1} amplifier stage that preserves the shape of the raw pulses (figure 2, left). The board's output signal was digitized by a TeledyneLeCroy HDO9409 digital oscilloscope operating at a bandwidth of 200 MHz and at a sampling rate of 1 GS s^{-1} (figure 2, center). Subsequent signal processing was done in the digital domain (figure 2, right). We first applied a correction for any (constant) electronic offsets, if these were

Table 1. A few scintillator properties as specified by major manufacturers, i.e. Luxium Solutions (formerly Saint Gobain Crystals) for LYSO:Ce and $LaBr_3$:Ce, and Crytur for YAP:Ce. The emission wavelength is that with the maximum intensity in the spectrum. The effective atomic number was calculated as $\sqrt[3.5]{\Sigma a_i Z_i^{3.5}}$, with a and Z the atomic weight fraction and the atomic number of the ith element in the material, respectively. This formula is valid if the photo-electric effect is the dominant interaction mechanism, which is the case for the materials and the energy range studied here ($E \leqslant 122$ keV).

	$Lu_{1.8}Y_{0.2}SiO_5$:Ce (LYSO:Ce)	$YAlO_3$:Ce (YAP:Ce)	$LaBr_3$:Ce
Decay time constant τ_d (ns)	36	25	16
Light yield Y (photons keV^{-1})	33	25	63
Emission wavelength (nm)	420	370	380
Mass density ρ (g cm^{-3})	7.1	5.4	5.1
Effective atomic number	65	33	46

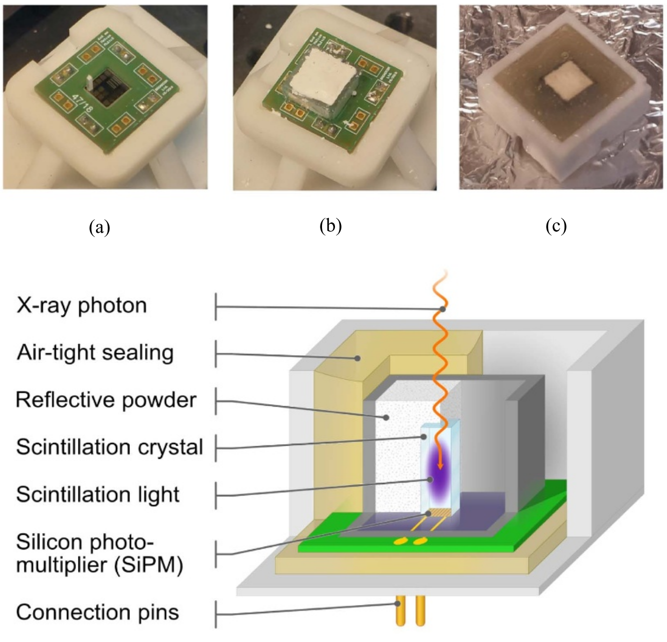
(a) (b) (c)

(d)

Figure 1. Overview of the assembly process of a single-pixel detector. (a) We first glued a scintillation crystal on a silicon photomultiplier (SiPM) using optically transparent glue. (b) Next, we covered the crystal in white polytetrafluoroethylene (PTFE, Teflon) powder, which was then compressed to increase reflectivity. (c) Only in the case of the hygroscopic LaBr$_3$:Ce scintillator, we additionally applied an air-tight epoxy sealing around the detector. (d) A schematic drawing of the fully assembled LaBr$_3$:Ce detector.

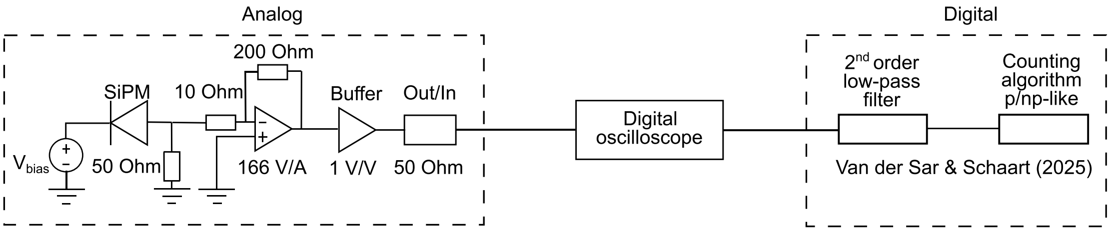

Figure 2. The detectors were mounted on Broadcom's AFBR-S4E001 evaluation board, which converts the current pulses from the SiPM into voltage pulses via a 166 V A^{-1} amplification stage, while preserving the raw pulse shapes. Through a buffer and a 50 Ω impedance, the voltage pulses were fed into and digitized by a TeledyneLeCroy HDO9409 digital oscilloscope operating at a bandwidth of 200 MHz and at a sampling rate of 1 GS s^{-1}. Subsequent signal processing was done in the digital domain. Details on the digital implementation of the second order low-pass filters and the (non)paralyzable-like counting algorithms can be found in Van der Sar and Schaart (2025) and in section 2.4 of this paper.

observed, to measurements conducted at low incident rate, i.e. with virtually no pile-up present. The exact same correction was then also applied to measurements at higher rates, so that possible additional baseline shifts due to pile-up at these higher rates were not corrected for. We subsequently applied a second-order low-pass filter with cut-off frequency f_c to suppress the statistical fluctuations on the pulses. The digital implementation of these filters is described in Van der Sar and Schaart (2025). Such fluctuations occur due to the finite number of scintillation photons detected per unit time, as explained in section 1. Figure 3 shows that filters with higher values of f_c lead to shorter pulses, which provide higher count rate capability, while they are less effective in suppressing the fluctuations on the pulses. Insufficient suppression will too often result in multiple counts for a single pulse, if a count is registered for every positive crossing of a predefined threshold, for example. Since we aim to push the rate capability in this work, we selected values of f_c that just sufficiently suppress the fluctuations. A value of 25 MHz turned out to be a suitable value of f_c for the LYSO:Ce and YAP:Ce detectors. In contrast, the raw pulses from the LaBr$_3$:Ce detector intrinsically have a lower level of statistical fluctuations, because this scintillator provides at least two times as many scintillation photons in about twice as short a time (see table 1). Figure 3 shows that this allowed f_c to be increased to 100 MHz for the LaBr$_3$:Ce detector, but not for the LYSO:Ce and YAP:Ce detectors.

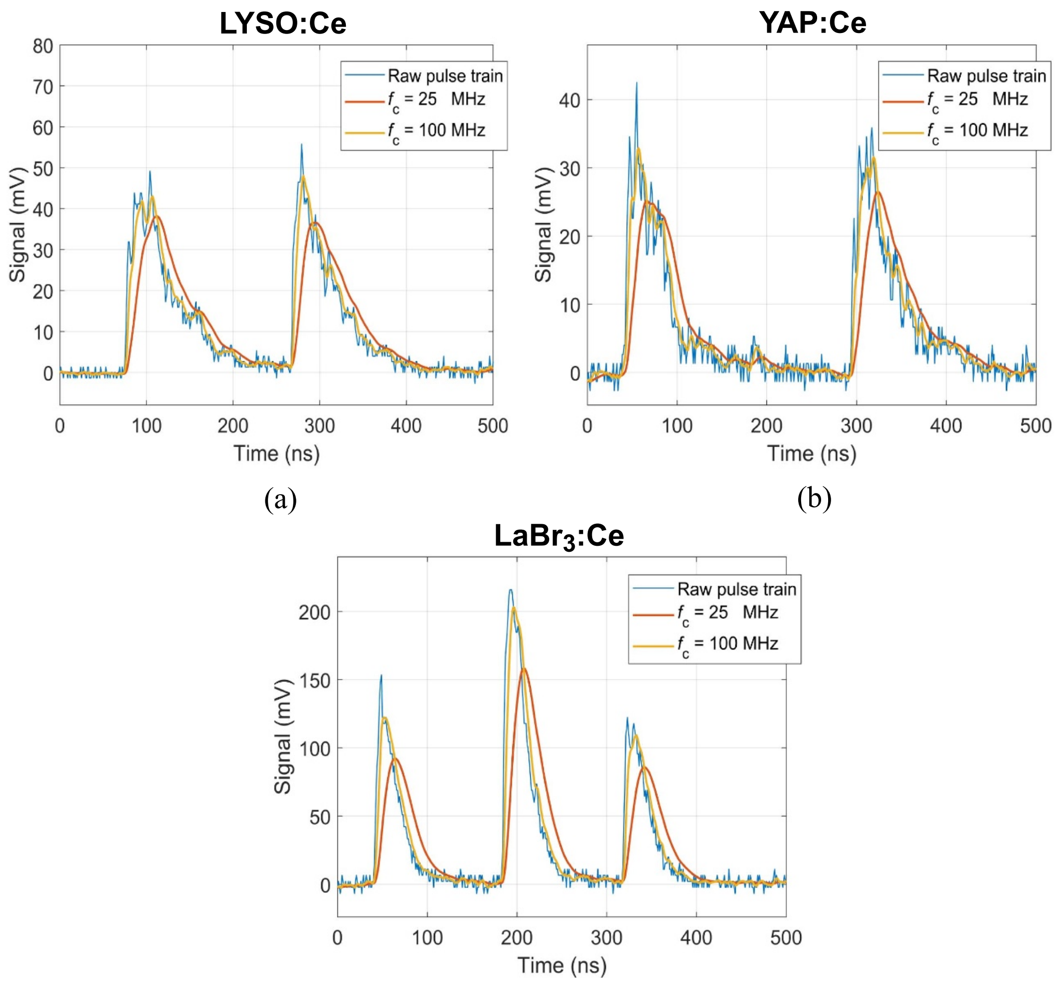

(a) (b)

(c)

Figure 3. The effect of applying second-order low-pass filters with different cut-off frequencies f_c on the raw pulse trains coming from (a) the LYSO:Ce detector, (b) the YAP:Ce detector, and (c) the LaBr$_3$:Ce detector. Higher values of f_c lead to shorter pulses, but are less effective in reducing the random fluctuations on the pulses. The figure shows that $f_c = 100$ MHz gives rise to smooth pulses in the case of the LaBr$_3$:Ce detector, but not in the case of the LYSO:Ce and YAP:Ce detectors. As such, $f_c = 100$ MHz can only be used for the LaBr$_3$:Ce detector.

2.3. Experiments using radioactive sources

We exposed each detector to three radioactive sources: Am-241 ($\sim10^2$ kBq), Ba-133 ($\sim10^2$ kBq), and Co-57 ($\sim10^3$ kBq) and recorded 10^5 pulses per combination of source and detector. We then applied second-order low-pass filters as described in section 2.2. For each filtered pulse, we determined the maximum signal, i.e. the pulse height, as a measure of the energy deposited. We used these data to construct pulse height histograms, in which we identified the full-energy peaks associated with the following photon emissions: 14 keV (Co-57), 32 keV (Ba-133), 60 keV (Am-241), 81 keV (Ba-133), and 122 keV (Co-57). It is noted that Ba-133 does not have a single gamma emission line at 32 keV, but emits a few narrowly spaced K x-rays, the emission yield-weighted average energy of which equals 32 keV. We determined the mean pulse height μ for each of the above-mentioned energies E from Gaussian fits to the measured full-energy peaks. We furthermore calculated the non-proportionality factor $f_{\text{non-pr}}$ with respect to the detector response at the highest energy of 122 keV as follows:

$$f_{\text{non}-\text{pr}}(E) = \frac{122\ \text{keV} \cdot \mu(E)}{\mu(122\ \text{keV}) \cdot E}. \tag{1}$$

The more $f_{\text{non-pr}}$ deviates from 1, the stronger the dependency of the scintillator's light yield on energy, which negatively affects the energy resolution (see section 1). We also calculated the low-rate full-width-at-half-maximum (FWHM) energy resolution R of each detector at $E = 60$ keV. We did so

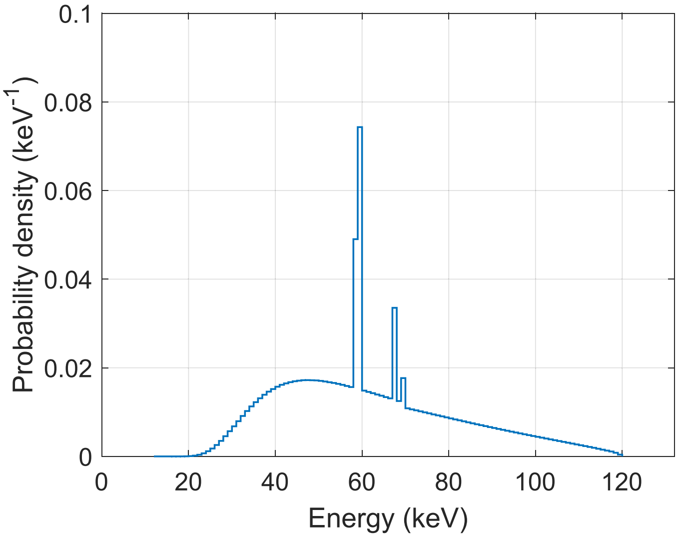

Figure 4. X-ray spectrum calculated by the SpekCalc software (Poludniowski *et al.* 2009) for an x-ray tube operating at a tube voltage of 120 kV, and having a tungsten target, an anode angle of 20°, and 3.0 mm Be and 7.5 mm Al filtration in total. This spectrum, which has a mean energy of 61.2 keV, was used in all experiments with an x-ray tube in this work.

from μ and the standard deviation σ obtained from the Gaussian fit to the full-energy peak in the Am-241 pulse height histogram in the following way:

$$R(E) = \frac{2.355 \cdot \sigma(E)}{\mu(E)} \cdot 100\%. \qquad (2)$$

2.4. Experiments using an x-ray tube

We also exposed each detector to an Yxlon Y.TU 320-D03 x-ray tube with a tungsten target and an anode angle of 20°. The sum of the intrinsic and added filtration was equal to 3.0 mm Be and 7.5 mm Al, and the tube voltage was set to 120 kV. The resulting spectrum, as calculated by the SpekCalc software (Poludniowski *et al* 2009), is shown in figure 4.

We gradually increased the tube current from the minimum value of 0.5 mA to the maximum value of 20 mA, while keeping the detector at a fixed distance from the source. This source-detector distance (SDD) was chosen such that hardly any pulse pile-up occurred in the measurement at 0.5 mA. We collected ten pulse trains of 100 ms for each tube current setting. These pulse trains were analyzed by means of a paralyzable-like (p-like) counting algorithm and a nonparalyzable-like (np-like) counting algorithm. Both algorithms make use of a count detection threshold, which we set to either 15 keV or 30 keV, covering the range of lowest-energy thresholds commonly applied in CdTe/CZT detectors. We determined the corresponding voltage levels by linear interpolation between the mean pulse heights measured at 14 keV and 32 keV with the radioactive sources (see section 2.3).

The p-like algorithm registers a count when the pulse train causes a positive threshold crossing. The maximum signal before the subsequent negative threshold crossing, which we refer to as the pulse height, is considered a measure of the energy associated with that count. The np-like algorithm, on the other hand, registers a count when a positive threshold crossing takes place, and evaluates whether or not the pulse train is still above threshold at the end of a window of duration τ_{np} following that threshold crossing. If so, a new count is registered and the evaluation is repeated a period of time τ_{np} later. This cycle is repeated until the outcome of the evaluation is negative. Then, the algorithm registers a new count when the next positive threshold crossing takes place. The maximum signal within τ_{np} (‘the pulse height’) is considered a measure of the energy associated with that count. In order to prevent counting single x-ray photons twice, it is crucial that $\tau_{\mathrm{np},x}$ for an x keV threshold exceeds the maximum time-over-the x keV threshold ($\mathrm{ToT}_{\mathrm{max},x}$) of the pulses. Figure 5 contains the five mean pulse shapes of events that ended up in the five full-energy peaks measured with the LaBr$_3$:Ce detector ($f_c = 100$ MHz) and the three radioactive sources mentioned in section 2.3. It shows that the larger the energy deposition in the scintillator, the larger ToT_x. Since the maximum photon energy in the x-ray tube experiments is 120 keV (see figure 4), we determined $\mathrm{ToT}_{\mathrm{max,15\,keV}}$ and $\mathrm{ToT}_{\mathrm{max,30\,keV}}$ for all detectors from the mean pulse shape of events that ended up in the 122 keV peak measured with the Co-57 source. We

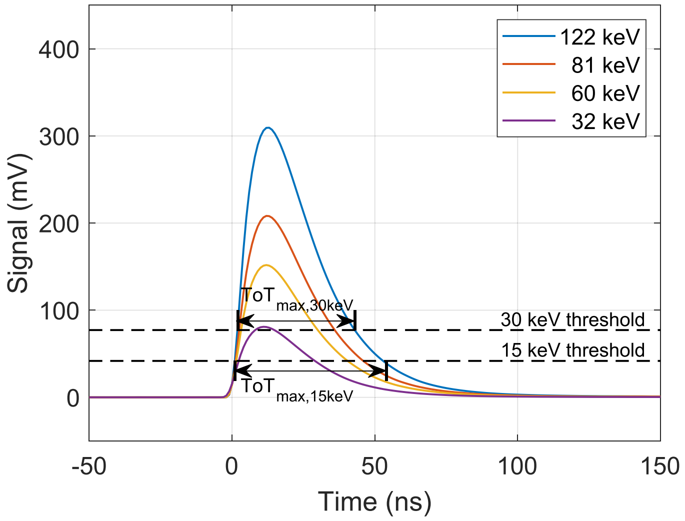

Figure 5. Mean shape of the pulses due to the full absorption of photons of various energies in the LaBr$_3$:Ce detector (f_c = 100 MHz). The 15 keV and 30 keV count-detection thresholds are also visualized, as well as the maximum time-over-the x keV thresholds ($\mathrm{ToT}_{\mathrm{max},x}$), i.e. the ToT_x for the 122 keV pulse. We chose τ_{np} values for the np-like counting algorithm that exceed these values of $\mathrm{ToT}_{\mathrm{max},x}$ (see table 2).

Table 2. The values of the parameter τ_{np} in the nonparalyzable-like counting algorithm for 15 keV and 30 keV count-detection thresholds, as used for the four combinations of scintillation material and cut-off frequency f_c in this work.

Scintillation material	f_c (MHz)	$\tau_{\mathrm{np,15\,keV}}$ (ns)	$\tau_{\mathrm{np,30\,keV}}$ (ns)
LYSO:Ce	25	130	100
YAP:Ce	25	100	80
LaBr$_3$:Ce	25	70	60
LaBr$_3$:Ce	100	55	45

then selected values of $\tau_{\mathrm{np,15\,keV}}$ and $\tau_{\mathrm{np,30\,keV}}$ that slightly exceed the values of $\mathrm{ToT}_{\mathrm{max},x}$ found in this way. These $\tau_{\mathrm{np},x}$ values are given in table 2.

Using a given combination of counting algorithm and threshold, we determined the number of counts in each of the ten pulse trains of 100 ms acquired at a certain tube current. We then calculated the output count rate (OCR) for each pulse train and averaged these OCRs to obtain a mean OCR at that tube current. We repeated this for each tube current in order to be able to plot a count rate curve, i.e. (mean) OCR as a function of tube current. However, it is more insightful to plot OCR as a function of input count rate (ICR). We therefore estimated an ICR for each tube current by assuming ICR = OCR for a tube current of 0.5 mA and a 15 keV threshold, and by making use of the fact that the ICR is proportional to the tube current. The former is a valid assumption, because we made sure there was hardly any pulse pile-up occurring at 0.5 mA and the minimum energy in the x-ray tube spectra exceeded 15 keV (see figure 4). We plot these estimated ICRs along the top horizontal axes of the count rate curve diagrams.

Furthermore, we show histograms of the pulse heights associated with the counts registered at the lowest ICR, i.e. at a tube current of 0.5 mA. These are the measured x-ray spectra. Using linear interpolation of the data on pulse height as a function of photon energy (see section 2.3), we plot x-ray energy along the top horizontal axes of these diagrams.

3. Results

3.1. Pulse height spectra of radioactive sources

Figures 6(a), (b) and (c) show the pulse height spectra of the three radioactive sources measured with the LYSO:Ce, YAP:Ce, and LaBr$_3$:Ce detectors, respectively.

The peaks resulting from the full absorption of 122 keV photons from the Co-57 source can be appreciated on the far right-hand side of the corresponding spectra. These peaks are typically accompanied by satellite peaks on their left-hand side, which represent photo-electric absorption events in which the resulting K x-ray escapes from the crystal. The average K x-ray energy equals 55 keV and 34 keV for the elements Lu and La, respectively, so this K-escape peak occurs at 67 keV in case of the

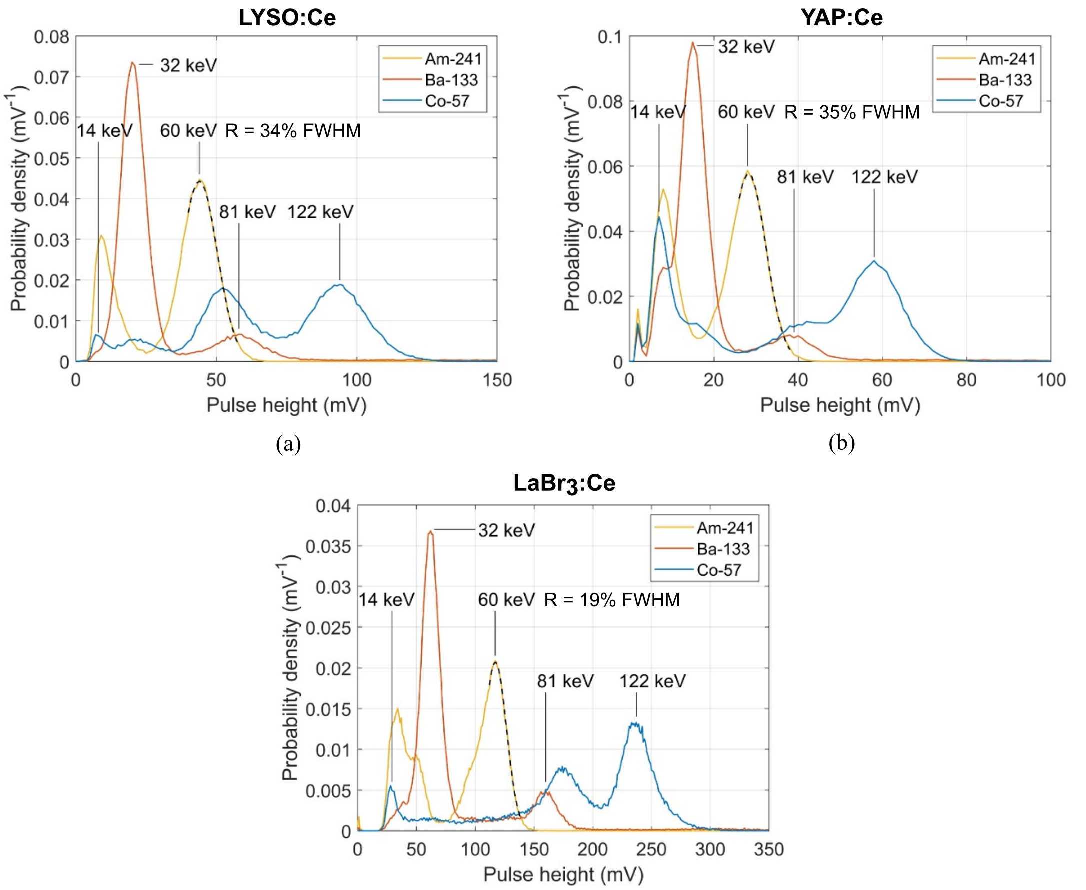

(a) (b)

(c)

Figure 6. Pulse height spectra of the Am-241, Ba-133, and Co-57 sources as measured with (a) the LYSO:Ce detector, (b) the YAP:Ce detector, and (c) the LaBr$_3$:Ce detector. All raw pulses were first filtered by a second-order low-pass filter with a cut-off frequency of 25 MHz before their pulse heights were determined. The dashed curves are Gaussian fits to the 60 keV peak, which were used to determine the full-width-at-half-maximum (FWHM) energy resolution. They run from 90% of the maximum on the left-hand side to 10% of the maximum on the right-hand side of the peak, in order to exclude the effect of the asymmetry of the peak on the energy resolution. The asymmetry is due to photons that have Compton scattered in the materials surrounding the scintillator (see figure 1) before being detected, as well as due to K-escape for some detectors.

LYSO:Ce detector (figure 6(a)) and at 88 keV in case of the LaBr$_3$:Ce detector (figure 6(c)). Yttrium K x-rays have an average energy of only 15 keV, so the counts in the Co-57 spectrum of the YAP:Ce detector (figure 6(b)) around 40 mV are too far away from the 122 keV peak to represent K-escape events. It is more likely that these are due to 122 keV photons that have Compton-scattered in the materials surrounding the scintillator, i.e. mainly in the compressed Teflon powder (with a low effective atomic number) in the case of the YAP:Ce detector (see figure 1(b)). The maximum energy loss due to Compton scattering in these materials is 39 keV for 122 keV photons, meaning that this continuum of counts starts at an energy of 83 keV. K x-rays from the lead shielding of the set-up (with an average energy of 77 keV) may also contribute to this continuum of counts. It is noted that similar counts have likely been registered by the LYSO:Ce and LaBr$_3$:Ce detectors, but they cannot be clearly resolved from the K-escape peaks in these cases.

Co-57 also emits 14 keV photons, giving rise to the indicated peaks on the left-hand side of the spectra. In the case of the YAP:Ce detector (figure 6(b)), this peak overlaps with what is likely a Compton plateau, which extends to 39 keV for incident photons with an energy of 122 keV. Because of the relatively low Z_{eff} of YAP:Ce (33, see table 1), Compton scattering is much more likely (37% of all interactions at 122 keV) than in LYSO:Ce and LaBr$_3$:Ce (6.6% and 15%, respectively). Thus, the corresponding features in figures 6(a) and (c), although present, are much weaker. Especially in the case of the LaBr$_3$:Ce detector (figure 6(c)), the Compton plateau is hardly visible, because it is spread out over many more 1 mV bins.

There is an additional feature, which is not only present in the Co-57 spectrum, but in all spectra measured with the YAP:Ce detector, namely the small peak at 2 mV (see figure 6(b)). This peak is due to SiPM dark counts, which generally constitute the main source of noise in SiPM-based detectors

(Piemonte and Gola 2019). It is noteworthy that there is hardly any overlap between this noise peak and the 14 keV peak, so dark counts can be simply and effectively rejected during data/image acquisition by setting the lowest threshold to a voltage level equivalent to at least 10 keV. The LYSO:Ce and LaBr$_3$:Ce detectors output stronger pulses in response to a single x-ray or gamma-ray photon (see figure 6), due to the higher light yield of these scintillators, for example (see table 1). The dark counts with a pulse height around 2 mV thus coincide with counts due to photons with an energy much less than 10 keV for these detectors. This means that a lowest threshold of far less than 10 keV is already sufficient to reject dark counts during acquisition. Indeed, we were able to set a trigger threshold on the digital oscilloscope that completely rejected the dark counts, without removing any part of the 14 keV peak. That is why the noise peak is absent in the spectra shown in figures 6(a) and (c).

The main peaks in the Ba-133 spectra are due to a narrow band of x-rays centered at 32 keV and a gamma-ray at 81 keV. Overlapping K-escape peaks can be seen on the left-hand side of the 32 keV peaks in figures 6(b) and (c). These are caused by the escape of bromine and yttrium K x-rays with average energies of 12 keV and 15 keV, respectively. In the LYSO:Ce detector (figure 6(a)), K-escape is negligible at an energy of 32 keV, because this energy is below the K-edge energy of Lu (63 keV). For photons with an energy of 81 keV, on the other hand, K-escape leads to an average energy deposition of 26 keV in the LYSO:Ce detector. As a result, the corresponding peak cannot be distinguished from the 32 keV peak. In the case of the YAP:Ce detector, the 81 keV peak is asymmetric because it overlaps with a K-escape peak around 66 keV. The K-escape peak lies at 47 keV in the case of the LaBr$_3$:Ce detector and contributes to the continuum of counts observed between the 32 keV and 81 keV peaks. Compton scattering of 81 keV photons in the low-Z_{eff} materials surrounding the LaBr$_3$:Ce crystal, such as the epoxy seal and the Teflon powder (see figures 1(b) and (c)), may further contribute to this continuum. For the LYSO:Ce and YAP:Ce detectors, this effect likely contributes to the asymmetric shape of the 81 keV full-energy peak.

In the case of the Am-241 source, the 60 keV full-energy peak is of main interest, because the other peak is due to a broad band of x-rays (11–22 keV). The spectrum measured with the LaBr$_3$:Ce detector (figure 6(c)) contains a lanthanum K-escape peak at 26 keV, which overlaps with the x-ray peak. The K-escape peak should be around 45 keV for the YAP:Ce detector, but cannot be distinguished from the 60 keV peak. Instead, it may contribute to the somewhat asymmetric shape of this peak (figure 6(b)). However, Compton scattering of 60 keV photons in the materials surrounding the scintillators, which leads to counts of at least 49 keV, also contributes to this asymmetry, given the clearly asymmetric shape of the 60 keV peak in the spectrum measured with the LaBr$_3$:Ce detector. K-escape from the LYSO:Ce crystal is again negligible for incident photon energies below the K-edge energy of 63 keV, so any asymmetry in the 60 keV peak in figure 6(a) can be due to Compton scattering, as well.

3.2. Energy resolution

The FWHM energy resolution of the 60 keV full-energy peak in an Am-241 spectrum is a commonly reported measure of spectral performance of x-ray PCDs. However, as discussed above and visualized in figure 6, counts due to photons that have Compton-scattered in low-Z_{eff} materials surrounding the crystal tend to make this peak asymmetric in our experiments. Meanwhile, such counts are unlikely in a pixel array, because Compton scattering hardly occurs in the investigated scintillation materials at 60 keV due to their higher Z_{eff}. We therefore tried to minimize the effect of these counts on the FWHM energy resolution. We did so by determining the energy resolution from a Gaussian fit to the 60 keV peak starting at 90% of the maximum on the left-hand side and extending till 10% of the maximum on the right-hand side of the peak (see figure 6). We thus found FWHM energy resolutions at 60 keV of 34% (LYSO:Ce, $f_c = 25$ MHz), 35% (YAP:Ce, $f_c = 25$ MHz), 19% (LaBr$_3$:Ce, $f_c = 25$ MHz), and 22% (LaBr$_3$:Ce, $f_c = 100$ MHz). A lower f_c leads to a somewhat better energy resolution for the LaBr$_3$:Ce detector, because it is more effective in reducing the pulse height variations among the pulses. Figure 6 furthermore shows that the superior energy resolution of the LaBr$_3$:Ce detector clearly provides better spectral separation between 60 keV and 81 keV photons, for example. This may allow for an additional energy bin in practice (see section 1), without too many photons being registered in a wrong bin.

3.3. Non-proportionality

We determined the (mean) pulse height and the non-proportionality factor $f_{\text{non-pr}}$ (see equation (1)) as a function of energy for each detector from the data presented in figure 6. The results are shown in figure 7. It can be observed that the LYSO:Ce detector is considerably less proportional than the YAP:Ce and LaBr$_3$:Ce detectors. Non-proportionality is a well-known characteristic of the LYSO:Ce scintillator itself (Khodyuk and Dorenbos 2012). The same holds for the remarkable behavior of $f_{\text{non-pr}}$ around the K-edge of lutetium at 63 keV. The relatively large deviation of $f_{\text{non-pr}}$ from 1 largely explains

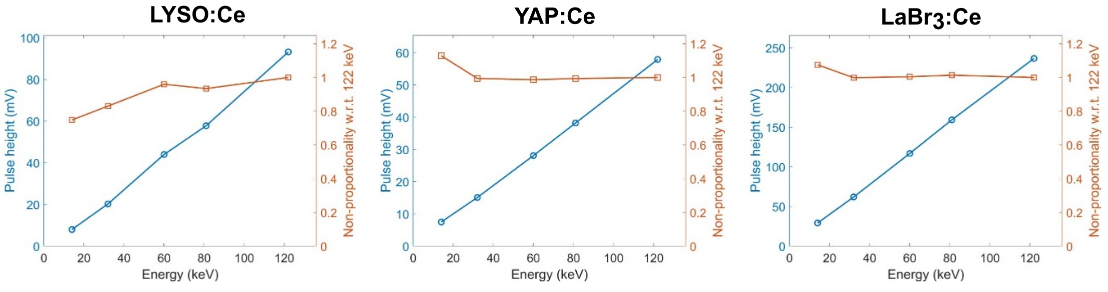

(a) (b) (c)

Figure 7. (Mean) pulse height as a function of energy, determined from Gaussian fits to the data in figure 6 for (a) the LYSO:Ce detector, (b) the YAP:Ce detector, and (c) the LaBr$_3$:Ce detector, with the cut-off frequency set to 25 MHz in all cases. The right axes show the non-proportionality factor $f_{\text{non-pr}}$ with respect to 122 keV, as defined in equation (1).

why the above-mentioned energy resolution of the LYSO:Ce detector is similar to that of the YAP:Ce detector despite a much stronger signal from the LYSO:Ce detector, i.e. more detected optical scintillation photons, caused by the higher light yield of LYSO:Ce, for example (see table 1). $f_{\text{non-pr}}$ only substantially deviates from 1 for the YAP:Ce and LaBr$_3$:Ce detectors around 14 keV. This deviation is in fact unexpected and may be related to the fact that $f_{\text{non-pr}}$ becomes sensitive to small errors in the fitted value of the mean pulse height when the photon energy becomes low compared with the reference energy of 122 keV (see equation (1)).

3.4. SiPM saturation

The proportional response of the YAP:Ce and LaBr$_3$:Ce detectors in the 30–120 keV range and the intrinsic non-proportionality of the LYSO:Ce scintillator, as shown in figure 7 and discussed in section 3.3, imply that SiPM saturation is negligible in these detectors and the measured energy resolutions in section 3.2 need not be corrected for it. Such a low level of saturation is also expected based on a detailed computational model of SiPM saturation applied to these detectors in our previous work (Van der Sar *et al* 2021, Van der Sar and Schaart 2021). Moreover, a first order estimate shows that even for the LaBr$_3$:Ce detector, which is most prone to saturation due to the relatively high number of optical photons detected per unit time, the saturation level remains low: That is, even if 120 keV (highest energy) $\times$ 63 photons keV^{-1} (light yield) $\times$ 0.5 (light collection efficiency) $\times$ 0.25 (PDE) $=$ 945 SPADs are triggered, this number of triggered SPADs is still much lower than the (1000 μm (pixel dimension)/15 μm (SPAD pitch))^2 $=$ 4444 SPADs available per pixel. Low saturation is therefore expected, especially considering that the SPAD recharge time constant is less than the scintillation decay time constant. See table 1 and section 2.1 for the parameter values used in this simple calculation of the saturation level.

3.5. X-ray tube spectra

Figure 8 shows the x-ray tube spectra measured with the three detectors, using the paralyzable-like counting algorithm with a 15 keV threshold, at the lowest tube current of 0.5 mA. The top horizontal axes show the energy in keV, derived from the data in figure 7. The tube voltage was 120 kV in all measurements. We notice little spectral overflow to energies above 120 keV, confirming that the pile-up level is low at this tube current. It is noted that the few counts registered above 120 keV can also result from the finite energy resolution of the detectors. Comparing the spectra in figure 8 to the ground truth in figure 4, we notice two main differences. Firstly, the K x-ray lines of the tungsten target are blurred. They are best resolved from the underlying Bremsstrahlung spectrum by the LaBr$_3$:Ce detector. This is in line with the observation that this detector offers the best energy resolution (see section 3.2). Secondly, the spectral intensity does not drop to zero around 20 keV, as expected based on figure 4. Registered counts around this energy are probably due to x-ray photons that first scatter in the materials surrounding the scintillation crystals (see figure 1) and x-ray photons that deposit only part of their energy in the scintillator during a Compton interaction. K-escape can also result in counts around 20 keV. For example, the high count rate registered by the LYSO:Ce detector at 15 keV (see figure 8(a)) may be due to K-escape following the photo-electric absorption of photons with an energy around 70 keV.

3.6. Count rate performance

Figure 9 shows the count rate curves obtained with the LYSO:Ce and YAP:Ce detectors. The curves for p-like counting indeed show paralyzable-like behavior, i.e. the OCR first reaches a maximum

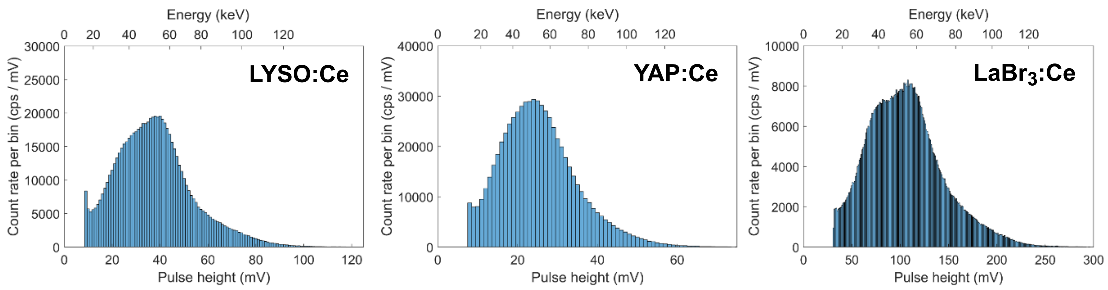

(a) (b) (c)

Figure 8. X-ray tube spectra measured with (a) the LYSO:Ce detector, (b) the YAP:Ce detector, and (c) the LaBr$_3$:Ce detector ($f_c = 25$ MHz). See figure 4 for a ground truth spectrum. The spectra shown here were acquired at a tube current of 0.5 mA, using a paralyzable-like counting algorithm with a 15 keV threshold. The conversion from pulse height (bottom horizontal axis) to energy (top horizontal axis) is based on the curves shown in figure 7.

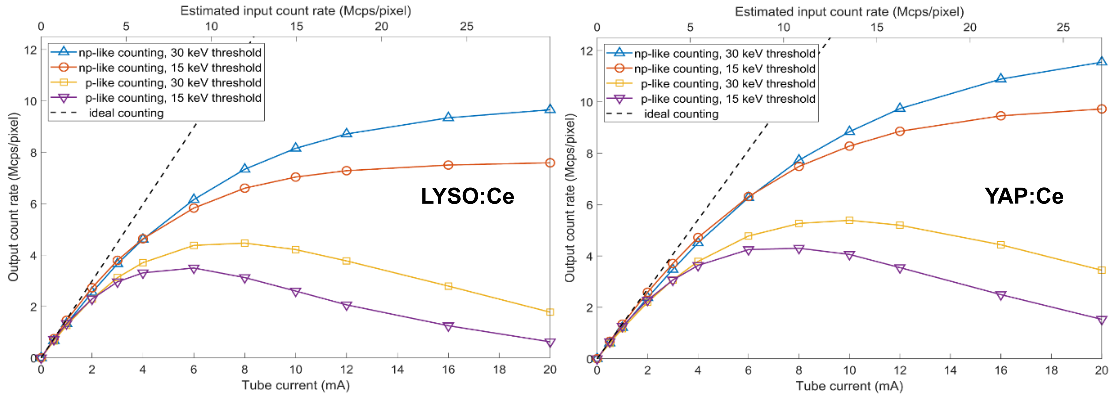

(a) (b)

Figure 9. Count rate curves, i.e. output count rate as a function of tube current (bottom horizontal axis) or (estimated) input count rate (top horizontal axis), for paralyzable-like (p-like) and nonparalyzable-like (np-like) counting algorithms and two low-energy count detection thresholds, measured with (a) the LYSO:Ce detector and (b) the YAP:Ce detector. The dashed line for ideal counting represents the case of the OCR equaling the estimated ICR.

before it decreases towards zero for increasing ICRs. The LYSO:Ce detector reaches maximum OCRs of 3.5 Mcps pixel^{-1} and 4.5 Mcps pixel^{-1} for 15 keV and 30 keV count detection thresholds, respectively, while the YAP:Ce detector achieves maximum OCRs of 4.3 Mcps pixel^{-1} and 5.4 Mcps pixel^{-1} for these thresholds. The corresponding estimated ICRs are about 2.5 times as large for both detectors. The detectors should only be used up to these values of ICR, so that the conversion of a measured OCR into an ICR, which is needed to determine the transmission of the object to be imaged, remains unambiguous. However, the closer the ICR to this maximally allowed ICR, the lower the contrast sensitivity.

Likewise, the curves for np-like counting show typical nonparalyzable behavior, i.e. they approach asymptotic values defined by OCR $= 1/\tau_{\mathrm{np}}$. The used values of τ_{np} were provided in table 2. In the case of the LYSO:Ce detector, the asymptotic values equal 7.7 Mcps pixel^{-1} and 10 Mcps pixel^{-1} for 15 keV and 30 keV thresholds, respectively. The curves for the YAP:Ce detector approach 10 Mcps pixel^{-1} and 12.5 Mcps pixel^{-1} for these thresholds. Since the curves do not have a maximum, there is no limit on the usable range of ICRs, although it again holds that the contrast sensitivity is lower in the flatter parts of the curves.

Comparing the results for the LYSO:Ce and YAP:Ce detectors, we observe that the latter performs somewhat better from a count-rate capability point-of-view. Not only the (slightly) faster decay time constant of YAP:Ce explains this observation, but also its more proportional energy response (see figures 7(a) and (b)). This can be understood as follows: If an x-ray photon with an energy of, say, 60 keV deposits its energy in a scintillator, the resulting detector pulse will be longer above the threshold when $f_{\mathrm{non\text{-}pr}}(E_{\mathrm{threshold}}) < f_{\mathrm{non\text{-}pr}}(60\ \mathrm{keV})$, compared to when $f_{\mathrm{non\text{-}pr}}(E_{\mathrm{threshold}}) \geqslant f_{\mathrm{non\text{-}pr}}(60\ \mathrm{keV})$ (also see equation (1)).

The count rate curves of the LaBr$_3$:Ce detector are shown in figure 10. For a cut-off frequency of 25 MHz (figure 10(a)) and p-like counting, we observe maximum OCRs of 6.0 Mcps pixel^{-1} and

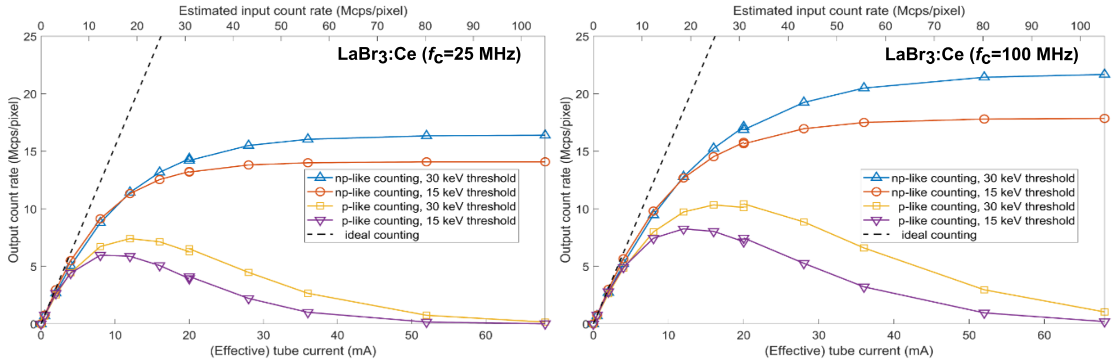

(a) (b)

Figure 10. Count rate curves, i.e. output count rate as a function of tube current (bottom horizontal axis) or (estimated) input count rate (top horizontal axis), for two counting algorithms and two low-energy thresholds, measured using the LaBr$_3$:Ce detector with (a) $f_c = 25$ MHz and (b) $f_c = 100$ MHz. The dashed line is the case of output count rate equaling input count rate.

7.4 Mcps pixel^{-1} for 15 keV and 30 keV thresholds, respectively. The corresponding estimated ICRs are about 2.5 times as large. The curves for np-like counting approach an asymptotic value just above 14.0 Mcps pixel^{-1} with a 15 keV threshold, and a value around 16.5 Mcps pixel^{-1} with a 30 keV threshold, in line with expectations based on calculating $1/\tau_{\mathrm{np}}$ for the values of τ_{np} listed in table 2.

Although the scintillation decay of LaBr$_3$:Ce is about twice as fast as that of LYSO:Ce and YAP:Ce, we do not yet observe twice as high OCRs. This is because we kept the cut-off frequency of the second-order low-pass filter at 25 MHz, which results in a substantial elongation of the pulses compared with the raw pulses (see figure 3(c)). Thus, to increase the rate capability by a factor of two, the time constant of the low-pass filter must also be reduced by a factor of two. Since f_c of a low-pass filter is inversely proportional to that time constant, an f_c of at least 50 MHz is needed. We showed in figure 4(c) that the high number of scintillation photons emitted and detected per unit time in the LaBr$_3$:Ce detector makes it even possible to increase f_c to 100 MHz. The count rate curves for $f_c = 100$ MHz are shown in figure 10(b). The maximum OCRs for p-like counting now increase to 8.3 Mcps pixel^{-1} and 10.4 Mcps pixel^{-1} for the 15 keV and 30 keV thresholds, respectively, while the curves for np-like counting approach 18 Mcps pixel^{-1} and 22 Mcps pixel^{-1} for the same two thresholds. Those values are indeed about twice as high as the corresponding values for the LYSO:Ce and YAP:Ce detectors, and again in line with expectations based on calculating $1/\tau_{\mathrm{np}}$ for the values of τ_{np} listed in table 2.

For completion, we note that the curves in figure 10 feature a small discontinuity at the maximum tube current of 20 mA. Since the LaBr$_3$:Ce detector in np-like counting mode appeared to be able to deal with considerably higher ICRs than could be reached with this tube current at the initial SDD, we performed additional measurements at a two-fold reduced SDD (which should yield a four-times as high ICR), starting a new tube current sweep at 5 mA (which should yield a four-times as low ICR). This is the reason why the horizontal axes in figure 10 are labeled *effective* tube current. The small discontinuities in the curves indicate that we did not manage to reduce the SDD by exactly a factor two.

4. Discussion

4.1. Single-pixel performance measurements

We measured the count rate curves and the low-fluence rate spectral performance, i.e. the proportionality of the energy response, the FWHM energy resolution at 60 keV, and the incident x-ray tube spectrum, of three 1×1 mm^2 single-pixel detectors consisting of either an LYSO:Ce, YAP:Ce, or LaBr$_3$:Ce scintillation crystal coupled to an ultrafast SiPM. Pulse processing consisted of current-to-voltage conversion, a second-order low-pass filter with cut-off frequency f_c optimized for counting performance rather than energy resolution, and either a paralyzable-like or nonparalyzable-like counting algorithm. Both algorithms consider pulse height as a measure of energy deposited.

As expected on the basis of scintillator characterization studies in literature (Khodyuk and Dorenbos 2012), the YAP:Ce and LaBr$_3$:Ce detectors showed a highly proportional response within the energy range investigated here (14 keV–122 keV). The LaBr$_3$:Ce detector achieved the best energy resolution at 60 keV of 19% FWHM for $f_c = 25$ MHz and 22% FWHM for $f_c = 100$ MHz. The former value is comparable to at least one CdTe detector developed for a diagnostic photon-counting CT (PCCT) prototype scanner of a major vendor (Steadman *et al* 2011). However, CdTe/CZT detectors developed with medical imaging applications in mind having energy resolutions at 60 keV of 4%–8% FWHM have also been reported (Steadman *et al* 2017, Zambon *et al* 2018, Thuering *et al* 2019).

A factor limiting the number of detected scintillation photons, and therefore the energy resolution, is the rather low (20%–30%) PDE of the SiPMs used here. This means that only 20%–30% of the scintillation photons incident on the SiPM are actually detected. However, an innovative, very fast (recharge time constant < 5 ns) SiPM with a PDE of 60% in the relevant wavelength range has already been reported (Engelmann *et al* 2020). This twice to thrice as high PDE can lead to a factor $\sqrt{2}$ to $\sqrt{3}$ better energy resolution. Especially the energy resolutions of detectors based on proportional scintillators, such as YAP:Ce and LaBr$_3$:Ce (see figure 7), are likely to benefit from a higher PDE. Thus, an energy resolution better than 15% FWHM at 60 keV may be feasible with a LaBr$_3$:Ce-based x-ray PCD. The best energy resolution at 60 keV measured with LaBr$_3$:Ce to date is 9.4% FWHM (Alekhin *et al* 2013).

In addition, we stress that the detectors presented in this work are prototypes. Further improvements in reflector and optical coupling between scintillator and SiPM may therefore be possible. These would also increase the number of detected scintillation photons, thereby contributing to the further improvement of the energy resolution.

Moreover, we opted for a few mm of compressed PTFE (Teflon) powder as a reflector around the scintillation crystal in this early stage of development. In the case of the hygroscopic LaBr$_3$:Ce detector, there was also an air-tight epoxy sealing around the detector (see figure 1). The 60 keV full-energy peaks, from which the energy resolutions were determined, were somewhat asymmetric, likely because some of the incident photons underwent Compton scattering in these surrounding materials with a low effective atomic number before hitting the crystal. This effect will be absent in a practical imaging detector, which primarily consists of a scintillation crystal array and typically contains relatively few low-Z_{eff} materials. Although we tried to mitigate the influence of the full-energy peak asymmetry on the energy resolution by fitting Gaussians only to the high-energy side of the peaks (see figure 6), the values of the energy resolution found in this way may still be worse than those obtained with a detector containing fewer low-Z_{eff} materials.

The best count rate performance in this work was obtained with the LaBr$_3$:Ce detector, using $f_{\mathrm{c}} = 100$ MHz. The scintillator's high light yield of 63 photons keV^{-1}, in combination with its short decay time constant τ_{d} of 16 ns, enables this high value of f_{c} by increasing the number of optical photons emitted and detected per unit time, thereby reducing the statistical fluctuations on the pulses (see section 2.2 and figure 3). When operated in p-like counting mode with a 30 keV threshold, the detector achieves a maximum OCR of 10.4 Mcps pixel^{-1}, while the OCR approaches an asymptotic value of 22 Mcps pixel^{-1} in np-like mode with the same threshold (see figure 10(b)). These values are about 80% of the corresponding values for two CdTe and CZT detectors developed for diagnostic PCCT (prototype) scanners of major vendors, namely 13 Mcps pixel^{-1} for p-like counting with a 30 keV threshold (Steadman *et al* 2017) and 28–29 Mcps pixel^{-1} for np-like counting with a 25 keV threshold (Kappler *et al* 2014), which corresponds to $\tau_{\mathrm{np}} \approx 35$ ns. Thus, equal count rate performance could be achieved at the imaging system level using only marginally smaller pixels. Moreover, we note that CdTe/CZT detectors with a lower maximum OCR of 4 Mcps pixel^{-1} in p-like mode (Zambon *et al* 2018), and an OCR approaching only 6.7 Mcps pixel^{-1} ($\tau_{\mathrm{np}} \approx 150$ ns), although with a pixel size of only 150 μm, in np-like mode (Thuering *et al* 2019) have been developed with medical applications in mind.

Given that the recharge time constant of the SiPM used in this work is less than the decay time constant of LaBr$_3$:Ce, higher OCRs per pixel could be achieved using a scintillator with $\tau_{\mathrm{d}} < 16$ ns. However, in order to benefit from a faster scintillation decay time constant, such a scintillator should have a sufficiently high light yield so that f_{c} need not be reduced to keep the pulse fluctuations at an acceptable level. It was shown in Van Blaaderen *et al* (2023) that benzylammonium lead bromide is a recently developed scintillator that meets this requirement. With $\tau_{\mathrm{d}} = 4.2$ ns, this scintillator can outperform CdTe/CZT in terms of rate capability. Note that the requirement on the light yield can be mitigated by using the aforementioned ultrafast SiPMs that have a higher PDE of 60%.

We note that it is not straightforward to make a fair and comprehensive comparison between our scintillation detectors and CdTe/CZT detectors. Firstly, because performance metrics depend on experimental conditions, pixel dimensions, and pulse processing, and, secondly, because basic performance measures, such as energy resolution and rate capability, do not appear to have been published for the most recent CdTe/CZT detectors developed for clinical systems. Nevertheless, the biggest difference between LaBr$_3$:Ce and CdTe/CZT detectors appears to lie in their energy resolutions, if measured in terms of the FWHM of the full-energy peak in a pulse-height spectrum measured at very low count rate.

In this context, it should be emphasized that the spectral performance of CdTe/CZT detectors is not only determined by their low-rate FWHM energy resolution, but also by inter-pixel crosstalk phenomena, in particular charge sharing (Taguchi *et al* 2024, Stierstorfer and Hupfer 2025).

The x-ray tube spectra measured with the scintillation detectors show a bump around the characteristic x-ray energies of tungsten (see figure 8). Despite the observation that scintillation detectors have a worse (LYSO:Ce and YAP:Ce) or at best similar ($LaBr_3$:Ce) FWHM energy resolution compared with CdTe/CZT detectors, this bump is typically weaker, or not present at all, in spectra acquired by CdTe/CZT detectors with sub-0.5 mm pixels for PCCT as a result of charge sharing. At lower energies, the intensity of the spectra measured with the scintillation detectors drops with decreasing energy (also see figure 8), as in the incident x-ray spectrum (see figure 4). This feature is typically also not present in spectra measured by CdTe/CZT detectors, again due to charge sharing (Taguchi *et al* 2024). Additionally, the measured radionuclide spectra (see figure 6) do not show the broad distribution of partial-energy events between 0 keV and the full-energy peak that is typically associated with charge sharing. It is noted that these beneficial features may be less prominent in spectra measured by scintillator pixel arrays with sub-0.5 mm pixels than in those of the single-pixel detectors studied here, due to light sharing between pixels (imperfect reflectors) and/or characteristic x-rays from neighboring pixels.

4.2. Insights from recent simulation studies

It is of interest to view the results of the presented single-pixel experiments in the context of recently published simulation studies that compare the performance of direct- and indirect-conversion materials for pixel arrays.

For example, an in-silico study by Stierstorfer and Hupfer (2025), comparing arrays of miniaturized CdTe and $LaBr_3$:Ce pixels, showed that in terms of the detective quantum efficiency for both non-spectral and spectral imaging tasks, such as water-iodine separation, $LaBr_3$:Ce detectors have the potential to outperform so-far realized CdTe detectors. Figure 6 in their paper clearly illustrates the importance of charge sharing in this regard: While in their work the modeled CdTe detector exhibits a better FWHM energy resolution than the $LaBr_3$:Ce detector, the fraction of events that fall outside the full-energy peak is much larger due to charge sharing in the case of the CdTe detector, resulting in a lower fraction of events being registered in the correct energy bin.

Moreover, another in-silico study by Taguchi *et al* (2024), comparing arrays of CdTe and $LaBr_3$:Ce with miniaturized pixels, showed that a $LaBr_3$:Ce detector potentially performs better than a CdTe detector in spectral imaging tasks, such as two- and three-material decomposition (K-edge imaging), due to the absence of charge sharing. Notably, they found that this holds over the whole range of fluence rates expected in diagnostic CT.

In our work, we have taken the first steps towards realizing an $LaBr_3$:Ce detector that can be used to demonstrate the potential benefits of fast scintillation detectors predicted by the two aforementioned simulation studies in benchtop imaging experiments. We have done so by constructing a single-pixel detector and showing that its counting and spectral performance are close to those found in literature for CdTe/CZT detectors developed for (prototype) diagnostic PCCT systems. These findings warrant the development of multi-pixel PCDs based on fast scintillators and the experimental assessment of their performance.

4.3. Outlook

In order to realize such a $LaBr_3$:Ce-based PCD, it is important that finely pixelated arrays are developed, with thin reflectors (well below 100 μm) in order to ensure high geometrical detection/dose efficiency. Examples of 38 μm to 65 μm thick reflectors can be found in, e.g. (Imai *et al* 2009), (Cherry and Qi 2012), (Godinez *et al* 2017), and (Shimazoe *et al* 2023).

Furthermore, it must be noted that $LaBr_3$:Ce is a hygroscopic material, requiring an air-tight sealing. Practical $LaBr_3$:Ce detectors are typically sealed using a thin layer of aluminum, as is the case for other hygroscopic scintillators, such as NaI:Tl. Such detectors are routinely applied in a variety of applications, including clinical applications, with expected life times exceeding 10 years. The other two scintillators investigated here, LYSO:Ce and YAP:Ce, have the benefit that they are not hygroscopic, but their energy resolutions exceed 30% FWHM at 60 keV and their maximum OCRs per pixel are approximately half of that of the $LaBr_3$:Ce detector (see figures 9 and 10(b)). Consequently, they would need about twice as many pixels per unit area to achieve a similar rate capability per mm^2, which comes with a number of drawbacks, such as increased inter-pixel crosstalk due to characteristic x-rays and lower geometrical dose efficiency for a given reflector thickness. Alternatively, the LYSO:Ce and YAP:Ce detectors may be useful for x-ray imaging systems that are less demanding in terms of rate capability and pixel size than diagnostic CT, such as cone-beam CT in (proton) radiotherapy (Van der Sar and Schaart 2025). Moreover, it also holds for the LYSO:Ce and YAP:Ce detectors that the aforementioned SiPMs with a PDE of 60% likely yield a better energy resolution and allow for a cut-off frequency exceeding 25 MHz, thereby reducing the pulse duration and improving the rate capability of these detectors.

5. Conclusion

The count rate curve and (low fluence rate) energy resolution are commonly used to describe the performance of x-ray photon-counting detectors for medical imaging applications. Here, we measured these parameters for three 1 × 1 mm^2 single-pixel detectors consisting of LYSO:Ce, YAP:Ce or $\mathrm{LaBr_3}$:Ce scintillation crystals coupled to ultrafast silicon photomultipliers.

The LYSO:Ce and YAP:Ce detectors reach maximum output count rates per pixel of about 40% of those found in literature for CdTe- and CZT-based direct-conversion detectors developed for (prototype) diagnostic photon-counting CT systems, while their energy resolutions exceed 30% FWHM at 60 keV. The $\mathrm{LaBr_3}$:Ce detector, on the other hand, achieves maximum OCRs of 10.4 Mcps pixel^{-1} and 22 Mcps pixel^{-1} in paralyzable-like and nonparalyzable-like counting mode, respectively. These numbers are about 80% of those of the above-mentioned direct-conversion detectors. Thus, equal count rate performance may be achieved at the imaging system level using marginally smaller pixels. Moreover, the $\mathrm{LaBr_3}$:Ce detector shows a proportional energy response, its energy resolution of about 20% FWHM at 60 keV is similar to that of at least one CdTe detector developed for a prototype diagnostic photon-counting CT system, and improvement to values better than 15% FWHM appears feasible. The x-ray tube spectra measured with the scintillation detectors represent the true incident x-ray spectrum reasonably well.

Our results indicate that $\mathrm{LaBr_3}$:Ce-based detectors may become a viable alternative for direct-conversion detectors for diagnostic PCCT, whereas LYSO:Ce- and YAP:Ce-based detectors appear more suitable for applications that are less demanding in terms of fluence rate, such as cone-beam CT in (proton) radiotherapy. Looking forward, further improvements in both counting and spectral performance are to be expected, if the SiPMs used here are replaced by SiPMs with a two to three times as high optical photon detection efficiency, which have already been developed. Moreover, research and development of faster scintillators than $\mathrm{LaBr_3}$:Ce with potential for photon-counting CT appears warranted, because such scintillators could outperform CdTe/CZT in terms of count rate capability.

Data availability statement

The data cannot be made publicly available upon publication because the cost of preparing, depositing and hosting the data would be prohibitive within the terms of this research project. The data that support the findings of this study are available upon reasonable request from the authors.

Acknowledgments

We thank Luxium Solutions (formerly Saint Gobain Crystals) for providing us with the 1 × 1 × 3 mm^3 $\mathrm{LaBr_3}$:Ce scintillation crystals. We also thank Broadcom Inc. for supplying the ultrafast SiPMs, and Stefan Brunner for sharing his experience with these SiPMs. Moreover, we appreciate fruitful discussions with Karl Stierstorfer about state-of-the-art CdTe/CZT detectors. Furthermore, we are grateful to Hugo van der Kort and Martin van Exter for designing the tools that allowed us to couple the small scintillators to the SiPMs. Lastly, we appreciate the help of Martijn de Boer and Jan Huizenga in setting up the experiments.

Disclosure

DL is funded by Varian, a Siemens Healthineers Company, Grant No. 2018016. SvdS and DS have no relevant conflicts of interest to disclose.

ORCID iDs

Stefan J van der Sar 0009-0004-6579-0047
David Leibold 0000-0001-7073-4075
Dennis R Schaart 0000-0002-3199-5608

References

Alekhin M S, De Haas J, Khodyuk I, Krämer K, Menge P, Ouspenski V and Dorenbos P 2013 Improvement of γ-ray energy resolution of $LaBr_3$:Ce^{3+} scintillation detectors by Sr^{2+} and Ca^{2+} co-doping *Appl. Phys. Lett.* **102** 161915

Bornefalk H and Danielsson M 2010 Photon-counting spectral computed tomography using silicon strip detectors: a feasibility study *Phys. Med. Biol.* **55** 1999

Cherry S R and Qi J 2012 High resolution PET with 250 micrometer LSO detectors and adaptive zoom (https://doi.org/10.2172/1032741)

Da Silva J, Grönberg F, Cederström B, Persson M, Sjölin M, Alagic Z, Bujila R and Danielsson M 2019 Resolution characterization of a silicon-based, photon-counting computed tomography prototype capable of patient scanning *J. Med. Imaging* **6** 043502

Danielsson M, Persson M and Sjölin M 2021 Photon-counting x-ray detectors for CT *Phys. Med. Biol.* **66** 03TR01

Dorenbos P, de Haas J T M and Van Eijk C 1995 Non-proportionality in the scintillation response and the energy resolution obtainable with scintillation crystals *IEEE Trans. Nucl. Sci.* **42** 2190–202

Engelmann E, Schmailzl W, Iskra P, Wiest F, Popova E and Vinogradov S 2020 Tip avalanche photodiode—a new generation silicon photomultiplier based on non-planar technology *IEEE Sens. J.* **21** 6024–34

Flohr T, Petersilka M, Henning A, Ulzheimer S, Ferda J and Schmidt B 2020 Photon-counting CT review *Phys. Med.* **79** 126–36

Godinez F, Gong K, Zhou J, Judenhofer M S, Chaudhari A J and Badawi R D 2017 Development of an ultra high resolution PET scanner for imaging rodent paws: PawPET *IEEE Trans. Radiat. Plasma Med. Sci.* **2** 7–16

Imai Y, Nukui M, Ishihara Y, Fujishige T, Ogata K, Moritake M, Kurochi H, Ogata T, Yahata M and Tang X 2009 Development and performance evaluation of an experimental fine pitch detector multislice CT scanner *Med. Phys.* **36** 1120–7

Kappler S, Henning A, Kreisler B, Schoeck F, Stierstorfer K and Flohr T 2014 Photon counting CT at elevated x-ray tube currents: contrast stability, image noise and multi-energy performance *Proc. SPIE* **9033** 368–75

Khodyuk I V and Dorenbos P 2012 Trends and patterns of scintillator nonproportionality *IEEE Trans. Nucl. Sci.* **59** 3320–31

Leng S, Bruesewitz M, Tao S, Rajendran K, Halaweish A F, Campeau N G, Fletcher J G and Mc Collough C H 2019 Photon-counting detector CT: system design and clinical applications of an emerging technology *RadioGraphics* **39** 729–43

Persson M, Bujila R, Nowik P, Andersson H, Kull L, Andersson J, Bornefalk H and Danielsson M 2016 Upper limits of the photon fluence rate on CT detectors: case study on a commercial scanner *Med. Phys.* **43** 4398–411

Piemonte C and Gola A 2019 Overview on the main parameters and technology of modern silicon photomultipliers *Nucl. Instrum. Methods Phys. Res. A* **926** 2–15

Poludniowski G, Landry G, Deblois F, Evans P and Verhaegen F 2009 SpekCalc: a program to calculate photon spectra from tungsten anode x-ray tubes *Phys. Med. Biol.* **54** N433

Rajendran K, Petersilka M, Henning A, Shanblatt E R, Schmidt B, Flohr T G, Ferrero A, Baffour F, Diehn F E and Yu L 2022 First clinical photon-counting-detector CT system: technical evaluation *Radiology* **303** 130

Roy U N, Camarda G, Cui Y, Gul R, Hossain A, Yang G, Zazvorka J, Dedic V, Franc J and James R 2019 Role of selenium addition to CdZnTe matrix for room-temperature radiation detector applications *Sci. Rep.* **9** 1–7

Sagisaka M, Toyoda T, Kataoka J, Arimoto M, Kawashima H, Kobayashi S, Murakami K, Okumura K, Sato D and Yoshiura K 2023 Experiment of *in vivo* imaging with third generation setup using photon-counting CT with 64ch multi-pixel photon counter *Nucl. Instrum. Methods Phys. Res. A* **1045** 167580

Schaart D R 2021 Physics and technology of time-of-flight PET detectors *Phys. Med. Biol.* **66** 09TR01

Shimazoe K, Kamada K, Yoshino M, Shoji Y, Sakamoto K, Acerbi F and Gola A 2023 Performance of custom fine-pitch SiPM-scintillator based photon counting detectors *2023 IEEE Nuclear Science Symp., Medical Imaging Conf. and Int. Symp. on Room-Temperature Semiconductor Detectors* p 1

Si-Mohamed S, Boccalini S, Rodesch P-A, Dessouky R, Lahoud E, Broussaud T, Sigovan M, Gamondes D, Coulon P and Yagil Y 2021 Feasibility of lung imaging with a large field-of-view spectral photon-counting CT system *Diagn. Interv. Imaging* **102** 305–12

Steadman R, Herrmann C and Livne A 2017 ChromAIX2: a large area, high count-rate energy-resolving photon counting ASIC for a spectral CT prototype *Nucl. Instrum. Methods Phys. Res. A* **862** 18–24

Steadman R, Herrmann C, Mülhens O and Maeding D G 2011 ChromAIX: fast photon-counting ASIC for spectral computed tomography *Nucl. Instrum. Methods Phys. Res. A* **648** S211–S215

Stierstorfer K and Hupfer M 2025 A Monte Carlo method to assess the spectral performance of photon counting detectors *Med. Phys.* **52** 1515–25

Surti S and Karp J S 2020 Update on latest advances in time-of-flight PET *Phys. Med.* **80** 251–8

Taguchi K, Schaart D R, Goorden M C and Hsieh S S 2024 Imaging performance of a $LaBr_3$:Ce scintillation detector for photon counting x-ray computed tomography: simulation study *Med. Phys.* **52** 158–70

Thuering T, Gkoumas S, Zambon P, Trueb P, Rissi M, Di Prima F, Donath T, Sawall S, Amato C and Kachelrieß M 2019 Towards large-area photon-counting detectors for spectral x-ray imaging *Med. Imaging* **10948** 290–5

Van Blaaderen J J, van der Sar S J, Onggo D, Sheikh M A K, Schaart D R, Birowosuto M D and Dorenbos P 2023 $(BZA)_2PbBr_4$: a potential scintillator for photon-counting computed tomography detectors *J. Lumin.* **263** 120012

Van der Sar S J, Brunner S E and Schaart D R 2021 Silicon photomultiplier-based scintillation detectors for photon-counting CT: a feasibility study *Med. Phys.* **48** 6324–38

Van der Sar S J, Brunner S E and Schaart D R 2022a x-ray photon-counting using silicon photomultiplier-based scintillation detectors at high x-ray tube currents *Proc. SPIE* **12031** 118–24

Van der Sar S J, Leibold D, Brunner S E and Schaart D R 2022b $LaBr_3$:Ce and silicon photomultipliers: towards the optimal scintillating photon-counting detector *7th Int. Conf. on Image Formation in X-ray Computed Tomography* vol 12304 pp 55–60

Van der Sar S J and Schaart D R 2021 Silicon photomultiplier-based scintillation detectors for photon-counting x-ray imaging *Radiation Detection Systems* (CRC Press) (https://doi.org/10.1201/9781003147633-10)

Van der Sar S J and Schaart D R 2025 Performance of x-ray photon-counting scintillation detectors under pile-up conditions at 60 keV *IEEE Trans. Radiat. Plasma Med. Sci.* **9** 708–20

Zambon P, Radicci V, Trueb P, Disch C, Rissi M, Sakhelashvili T, Schneebeli M and Broennimann C 2018 Spectral response characterization of CdTe sensors of different pixel size with the IBEX ASIC *Nucl. Instrum. Methods Phys. Res. A* **892** 106–13